Introducing the monoclinic polymorph of the honeycomb magnet Na$_2$Co$_2$TeO$_6$

Emilie Dufault,[1,*] Faranak Bahrami ●,[1,*] Alenna Streeter,[1] Xiaohan Yao ●,[1] Enrique Gonzalez ●,[1]
Qiang Zhang ●,[2] and Fazel Tafti ●[1,†]

[1]*Department of Physics, Boston College, Chestnut Hill, Massachusetts 02467, USA*
[2]*Neutron Scattering Division, Oak Ridge National Laboratory, Oak Ridge, Tennessee 37830, USA*

Recent theoretical studies have suggested that the low-energy Hamiltonian of honeycomb cobaltate systems could be dominated by anisotropic Kitaev interactions. Motivated by the theory, a honeycomb layered material Na$_2$Co$_2$TeO$_6$ with a hexagonal unit cell has been studied and found to exhibit antiferromagnetic (AFM) ordering at 27 K with two spin reorientation transitions at 15 and 5 K. Here we report a monoclinic polymorph of Na$_2$Co$_2$TeO$_6$, also with honeycomb layered structure but with a single AFM transition at 9.6 K and without spin reorientation transitions at lower temperatures. Using neutron diffraction, we identify an in-plane zigzag AFM order in the ground state with the spins canted out of the honeycomb planes and ferromagnetically coupled between them. The zigzag order is suppressed by a magnetic field of 6 T. The lower critical temperature and field, positive Curie-Weiss temperature, and out-of-plane canting of spins in the monoclinic Na$_2$Co$_2$TeO$_6$ suggest enhanced frustration in this polymorph compared to the hexagonal one.

I. INTRODUCTION

Establishing a quantum spin liquid (QSL) phase is highly desired in condensed matter physics, since the non-Abelian anyonic excitations of a QSL can be used as qubits for topological quantum computing [1–6]. One of the most promising proposals for the QSL phase is the Kitaev model based on anisotropic interactions among spin-1/2 particles on a honeycomb lattice [7]. Experimental efforts to materialize the Kitaev model have been largely focused on honeycomb layered structures with heavy transition metals such as α-Li$_2$IrO$_3$, Na$_2$IrO$_3$, Li$_2$RhO$_3$, α-RuCl$_3$, Cu$_2$IrO$_3$, Ag$_3$LiIr$_2$O$_6$, Ag$_3$LiRh$_2$O$_6$, Cu$_3$LiIr$_2$O$_6$, and H$_3$LiIr$_2$O$_6$ [8–24]. The choice of $4d$ and $5d$ transition metals (Ru, Rh, Ir) is due to their strong spin-orbit coupling (SOC) that induces anisotropic interactions among pseudospin-1/2 ($J_{\text{eff}} = 1/2$) spin-orbital states [25–27]. Such $J_{\text{eff}} = 1/2$ Kramers doublets originate from the low-spin configuration $t_{2g}^5 e_g^0$ of the $(4, 5)d^5$ orbitals of Ru^{3+}, Rh^{4+}, and Ir^{4+} subjected to octahedral crystal electric field (CEF) [28].

Recent theoretical studies have suggested that both the anisotropic exchange interactions and Kramers doublets can also be realized in the high-spin configuration $t_{2g}^5 e_g^2$ of the $3d^7$ orbitals of Co^{2+} and Ni^{3+} [29–32]. The tantalizing possibility of synthesizing Kitaev QSL candidate materials with earth-abundant elements (Co and Ni) instead of precious metals (Ru, Rh, and Ir) led to a surge of activity on such materials as Na$_3$Co$_2$SbO$_6$ and Na$_2$Co$_2$TeO$_6$ [33–40]. In these compounds, anisotropic interactions stem from a sizable Hund's coupling

in the e_{g} manifold and enhanced SOC effect of the ligands due to proximity of oxygen to heavier Sb or Te atoms [31].

Na$_3$Co$_2$SbO$_6$ crystallizes in the monoclinic space group $C2/m$ similarly to the iridates. It undergoes antiferromagnetic (AFM) ordering at $T_{\text{N}} = 8.3$ K. Reports of both positive and negative Curie-Weiss temperature depending on the sample quality and fitting range suggest a competition between ferromagnetic (FM) and AFM interactions in this material [33–35]. Na$_2$Co$_2$TeO$_6$ instead crystallizes in the hexagonal space group $P6_322$. It undergoes an AFM transition at 27 K followed by two spin reorientation transitions at 15 and 5 K. The negative $\Theta_{\text{CW}} = -8.3$ K in polycrystalline samples confirms dominant AFM interactions, unlike competing FM and AFM interactions found in Na$_3$Co$_2$SbO$_6$ [37–40].

Both the monoclinic ($C2/m$) unit cell of Na$_3$Co$_2$SbO$_6$ and hexagonal ($P6_322$) unit cell of Na$_2$Co$_2$TeO$_6$ possess sodium disorder between the honeycomb layers. However, there is more disorder in the hexagonal structure because it allows for three interlayer Wyckoff sites unlike the monoclinic structure with two interlayer Wyckoff sites according to powder x-ray refinements. Such disorder in the interlayer site occupancy randomizes the position of oxygen atoms and leads to higher levels of bond randomness within the honeycomb layers and stacking faults between them [Fig. 1(a)].

In this article, we introduce a monoclinic polymorph of Na$_2$Co$_2$TeO$_6$ in the space group $C2/m$, which is structurally similar to Na$_3$Co$_2$SbO$_6$. As shown in Fig. 1, the two-layer monoclinic polymorph reported here has a smaller amount of interlayer sodium disorder than the three-layer hexagonal polymorph [36,37,39,40]. Unlike the hexagonal Na$_2$Co$_2$TeO$_6$ that has three transitions at 27, 15, and 5 K, the monoclinic polymorph has a single AFM transition at 9.6 K. Also, the large splitting between zero-field-cooled (ZFC) and field-cooled (FC) susceptibility in the hexagonal Na$_2$Co$_2$TeO$_6$,

---

*These authors contributed equally to this work.
†fazel.tafti@bc.edu
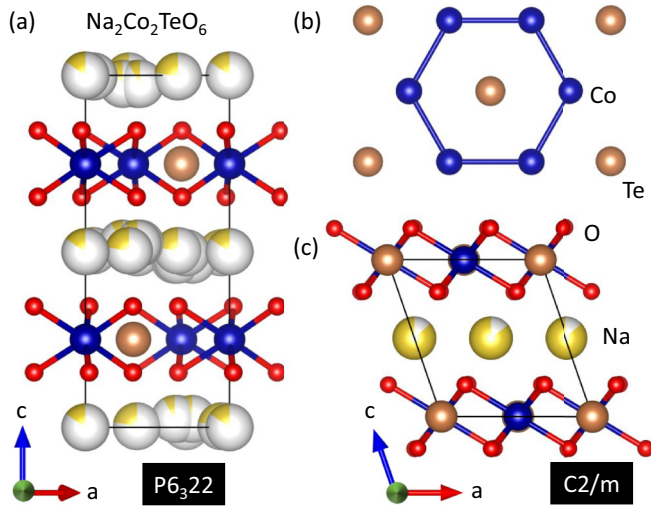
FIG. 1. (a) The hexagonal polymorph of $Na_2Co_2TeO_6$ has considerable sodium deficiency and site disorder between the layers. The yellow and white colors show Na occupancy and vacancy, respectively. (b) Both hexagonal ($P6_322$) and monoclinic ($C2/m$) space groups have honeycomb layers. (c) The monoclinic polymorph has less interlayer sodium disorder.

indicative of spin-glass behavior, is absent in the monoclinic polymorph consistent with lower disorder levels. Our findings suggest enhanced magnetic frustration in the monoclinic $Na_2Co_2TeO_6$ compared to its hexagonal polymorph. However, further studies are required to determine whether the ground state of the title compound fits a Kitaev or XXZ model [41,42]. The latter seems to be a better description of the magnetic properties of most Co^{2+} honeycomb systems [43–46]. We discuss this issue toward the end of the article.

II. EXPERIMENTAL METHODS

Polycrystalline samples of both hexagonal and monoclinic $Na_2Co_2TeO_6$ were synthesized via a solid-state reaction. The precursors, sodium carbonate (99.5%), cobalt oxide (99.7%), and tellurium oxide (99.99%), were mixed and reacted according to the following equation:

$$3Na_2CO_3 + 2Co_3O_4 + 3TeO_2 \rightarrow 3Na_2Co_2TeO_6. \quad (1)$$

The mixture was pressed into a 350 mg pellet, wrapped in a gold foil, and sintered in a capped alumina crucible at $850\,^\circ$C for 24 h. It was then cooled to $550\,^\circ$C and quenched in a dry box. The hexagonal polymorph was obtained by following Eq. (1) strictly, and the monoclinic polymorph was obtained by adding 30% molar excess of Na_2CO_3. Both polymorphs were stable in air and had distinguishable colors of purple (monoclinic) and maroon (hexagonal) as shown in Fig. 2. We also synthesized the nonmagnetic analog $Na_2Zn_2TeO_6$ with a similar approach (using 50% additional Na_2CO_3) to subtract the phonon background from the heat capacity data.

Powder x-ray diffraction (PXRD) measurements were performed using a Bruker D8 ECO instrument with a Cu-Kα source. The FullProf suite [47] and VESTA software [48] were used for the Rietveld refinements and crystal
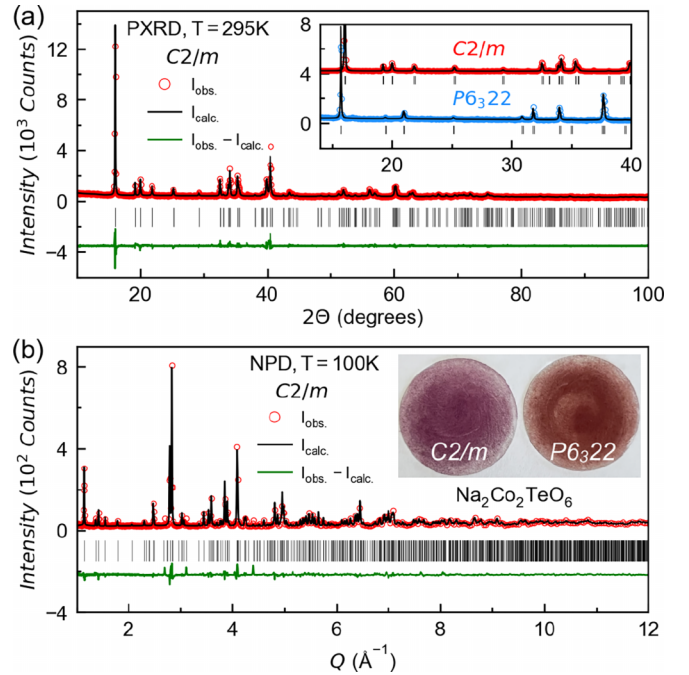

FIG. 2. (a) Rietveld refinement of the PXRD pattern of monoclinic $Na_2Co_2TeO_6$. The inset compares PXRD patterns of the monoclinic ($C2/m$) and hexagonal ($P6_322$) polymorphs. (b) Rietveld refinement of the NPD pattern at $T \gg T_N$. The inset compares the colors of the monoclinic (purple) and hexagonal (maroon) polymorphs.

visualizations. Magnetization and heat capacity measurements were performed using a Quantum Design MPMS3 and PPMS Dynacool, respectively. Neutron powder diffraction (NPD) was performed on the time-of-flight (TOF) powder diffractometer POWGEN at the Spallation Neutron Source at Oak Ridge National Laboratory by loading 2.5 g of dried powder into a vanadium sample can and cooling it in an orange cryostat. For optimal nuclear and magnetic refinements, two neutron banks with center wavelengths of 1.500 Å and 2.556 Å were selected, respectively, at 100 K and 1.6 K. The FullProf **k**-Search software was used to identify the magnetic propagation vector [47]. The Bilbao Crystallographic Server [49] was used for the magnetic symmetry analysis, and GSAS-II [50] was used for the refinements.

III. RESULTS AND DISCUSSION

A. Structural analysis

Figures 2(a) and 2(b) show the PXRD and NPD patterns of the monoclinic polymorph of $Na_2Co_2TeO_6$ (red empty circles) with Rietveld refinements in the $C2/m$ space group (black solid lines). The crystallographic solution confirmed by both PXRD and NPD is visualized in Figs. 1(b) and 1(c), and the refinement details are summarized in Appendix A. The inset of Fig. 2(a) shows visible differences between the PXRD patterns of the monoclinic ($C2/m$) and hexagonal ($P6_322$) polymorphs. The first peak of the hexagonal compound is located at a lower angle compared to that of the monoclinic compound suggesting a stronger interlayer connection and
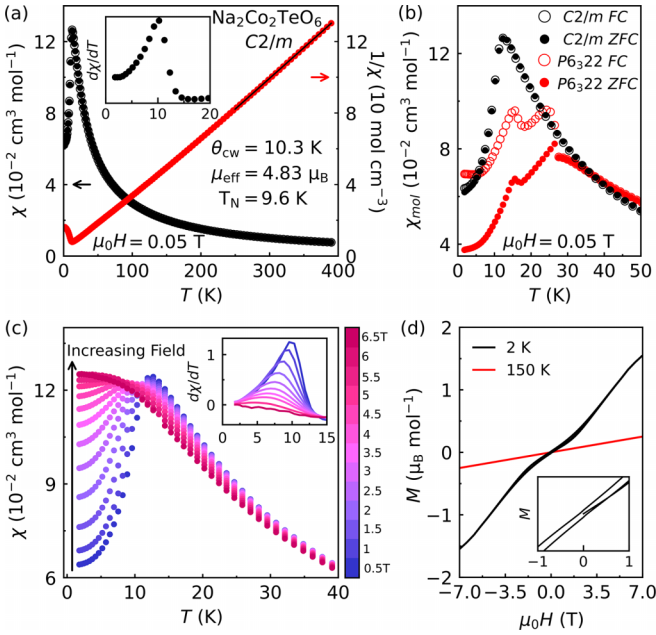
FIG. 3. (a) Magnetic susceptibility per mole Co (black) and inverse susceptibility (red) plotted as a function of temperature. The filled and empty circles correspond to zero-field-cooled (ZFC) and field-cooled (FC) data, respectively. The solid black line is a Curie-Weiss (CW) fit above 250 K. Inset shows the $d\chi/dT$ curve to identify T_N. (b) Comparison between $\chi(T)$ in the monoclinic and hexagonal polymorphs of $Na_2Co_2TeO_6$. (c) $\chi(T)$ (and $d\chi/dT$ in the inset) at several fields. (d) Magnetization as a function of field at 2 and 150 K. Inset shows a weak hysteresis at small fields.

smaller interlayer spacing in the monoclinic polymorph. The inset of Fig. 2(b) shows that the two polymorphs have different colors. As shown in Fig. 1, the amount of Na deficiency between the layers of monoclinic $Na_2Co_2TeO_6$ is significantly less than that of the hexagonal polymorph—a direct result of the change of space group. Therefore, structural disorders such as bond randomness within the honeycomb layers and stacking faults between them are fewer in the newly synthesized monoclinic polymorph.

B. Magnetic characterization

The monoclinic polymorph of $Na_2Co_2TeO_6$ has a single AFM transition characterized by one peak in the susceptibility data $\chi(T)$ without ZFC/FC splitting [Fig. 3(a)]. The Néel temperature $T_N = 9.6(6)$ K is determined from the peak in $d\chi/dT$ in the inset of Fig. 3(a). A comparison between the $\chi(T)$ curves of the monoclinic and hexagonal polymorphs is shown in Fig. 3(b). The hexagonal polymorph orders at a higher temperature $T_N = 27$ K with two spin reorientation transitions at 15 and 5 K, corresponding to the peak and trough in the ZFC data, as reported in prior works [37,39,40]. Such features are absent in the monoclinic polymorph. Figure 3(b) also shows the absence (presence) of ZFC/FC splitting in the monoclinic (hexagonal) polymorph indicating the absence (presence) of spin-glass behavior consistent with less (more) Na disorder. In Appendix B we show that a lower-quality sample of the monoclinic $Na_2Co_2TeO_6$ has a

TABLE I. Magnetic properties of $Na_3Co_2SbO_6$ and the hexagonal and monoclinic polymorphs of $Na_2Co_2TeO_6$ (polycrystalline samples).

	$Na_2Co_2TeO_6$ Hexagonal	$Na_3Co_2SbO_6$ Monoclinic	$Na_2Co_2TeO_6$ Monoclinic
Space group	$P6_322$	$C2/m$	$C2/m$
T_N	27 K	8.3 K	9.6 K
Θ_{CW}	-8.3 K	-0.8 to $+2.2$ K	$+10.3$ K
μ_{eff}	5.34 μ_B	5.22 μ_B	4.83 μ_B
S_m/Co	0.70 $R\ln(2)$	1.47 $R\ln(2)$	0.70 $R\ln(2)$
Reference	[37,38]	[33,34]	this work

lower transition temperature (5.9 K instead of 9.6 K) with an upturn around 3 K. These observations suggest that the previously reported spin re-orientation transitions in hexagonal $Na_2Co_2TeO_6$ [37–40] may be due to an impurity phase of the monoclinic polymorph.

A Curie-Weiss (CW) analysis, $\chi^{-1} = (T - \Theta_{CW})/C$, at $T > 250$ K in Fig. 3(a) yields a CW temperature of $\Theta_{CW} = +10.3$ K and an effective moment of $\mu_{eff} = 4.83$ μ_B. The positive sign of Θ_{CW} in the monoclinic $Na_2Co_2TeO_6$ indicates the presence of FM correlations, unlike in the hexagonal $Na_2Co_2TeO_6$ which has a negative CW temperature ($\Theta_{CW} = -8.3$ K). Both positive and negative values of Θ_{CW} have been reported for $Na_3Co_2SbO_6$ which has a monoclinic structure ($C2/m$) and exhibits an AFM order at $T_N = 8.3$ K [33–35]. In this regard, the behavior of $Na_3Co_2SbO_6$ is intermediate between the hexagonal and monoclinic polymorphs of $Na_2Co_2TeO_6$. Table I summarizes the magnetic parameters of these materials.

The effective moment of 4.83 μ_B in the monoclinic $Na_2Co_2TeO_6$ is close to the value 4.73 μ_B expected from a high-spin $3d^7$ system with $S = 3/2$ and $L_{eff} = 1$ with unquenched orbital moment ($g = 1.6$ instead of 2). The effective moments of hexagonal $Na_2Co_2TeO_6$ (5.34 μ_B) and $Na_3Co_2SbO_6$ (5.22 μ_B) are slightly higher than this value (Table I).

Figure 3(c) shows that T_N, defined as the peak in $d\chi/dT$, is suppressed by an external magnetic field of 6 T. A similar behavior is observed in the hexagonal polymorph, where the suppression of T_N happens at 9 T [39]. Such a behavior is reminiscent of the field-induced quantum paramagnetic phase proposed for α-$RuCl_3$ [51].

Figure 3(d) shows magnetization curves below and above T_N in the monoclinic $Na_2Co_2TeO_6$. Unlike the hexagonal polymorph [33] that shows a saturation of magnetization at 3 T, the monoclinic polymorph requires a larger field to saturate magnetization, possibly due to a stronger magnetocrystalline anisotropy. The inset of Fig. 3(d) shows a weak hysteresis at 2 K for $H < 3$ T, evidence of a finite FM component, and competing FM/AFM interactions. This is consistent with the observed positive Θ_{CW} despite AFM ordering (Table I) as well as the c-type zigzag AFM order found by neutron scattering (Sec. III D).
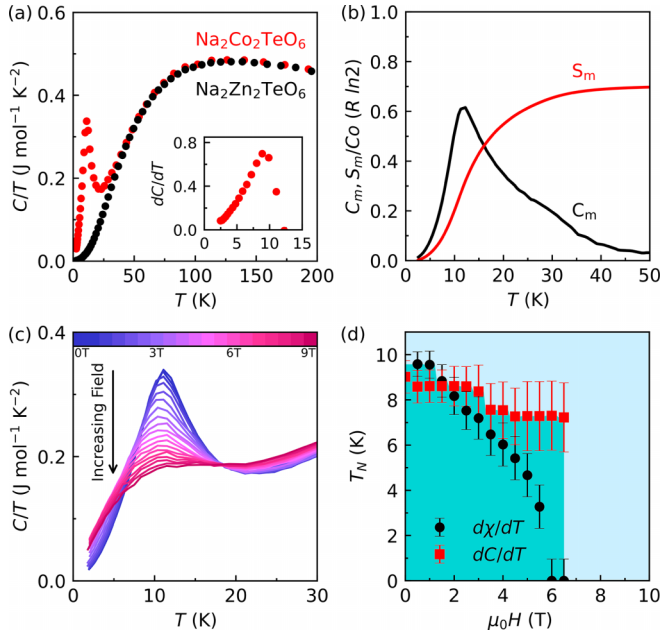
FIG. 4. (a) Heat capacity divided by temperature (C/T) per mole Co or Zn plotted as a function of temperature for monoclinic $Na_2Co_2TeO_6$ (red) and $Na_2Zn_2TeO_6$ (black). The black data is multiplied by 0.95 to correct for the mass difference between Co and Zn. Inset shows dC/dT at zero field to determine T_N. (b) Magnetic heat capacity (C_m) and entropy (S_m) of monoclinic $Na_2Co_2TeO_6$ in units of $R\ln(2)$ as a function of temperature. (c) C/T per mole Co as a function of temperature at different magnetic fields. (d) Suppression of T_N with increasing field according to $d\chi/dT$ and dC/dT data. Error bars correspond to the width of peaks at 90% maximum below 4 T.

C. Heat capacity

Similar to the magnetic susceptibility data, a single peak is observed at 12 K in the heat capacity of monoclinic $Na_2Co_2TeO_6$ due to AFM ordering [Fig. 4(a)]. The low-temperature spin reorientation transitions found in the hexagonal $Na_2Co_2TeO_6$ are absent in the monoclinic polymorph according to both magnetic susceptibility and heat capacity data [Figs. 3(a) and 4(a)]. The peak in dC/dT in the inset of Fig. 4(a) is used to evaluate $T_N = 9.6(6)$ K consistent with the value reported from $d\chi/dT$ in the inset of Fig. 3(a). The lower T_N in the monoclinic polymorph (9.6 K) compared to hexagonal polymorph (27 K) indicates enhanced magnetic frustration due to the change of crystal symmetry (Fig. 1).

To isolate the magnetic heat capacity, we synthesized monoclinic $Na_2Zn_2TeO_6$ (a nonmagnetic isostructural analog of the title compound) and measured its purely phononic heat capacity [black data in Fig. 4(a)]. After subtracting the phonon background, the magnetic heat capacity (C_m/T) is plotted in units of $R\ln(2)$ per mole Co in Fig. 4(b) (black curve). Also, the magnetic entropy is calculated by numerical integration using $S_m = \int (C_m/T)dT$ and plotted in Fig. 4(b) (red curve). It reaches 70% of $R\ln(2)$, which is the expected molar entropy per Co^{2+} for the theoretically predicted Γ_7 doublet (pseudospin-1/2) [52]. Releasing 70% of this amount across the AFM transition could be due to either an incomplete phonon subtraction or considerable fluctuations of
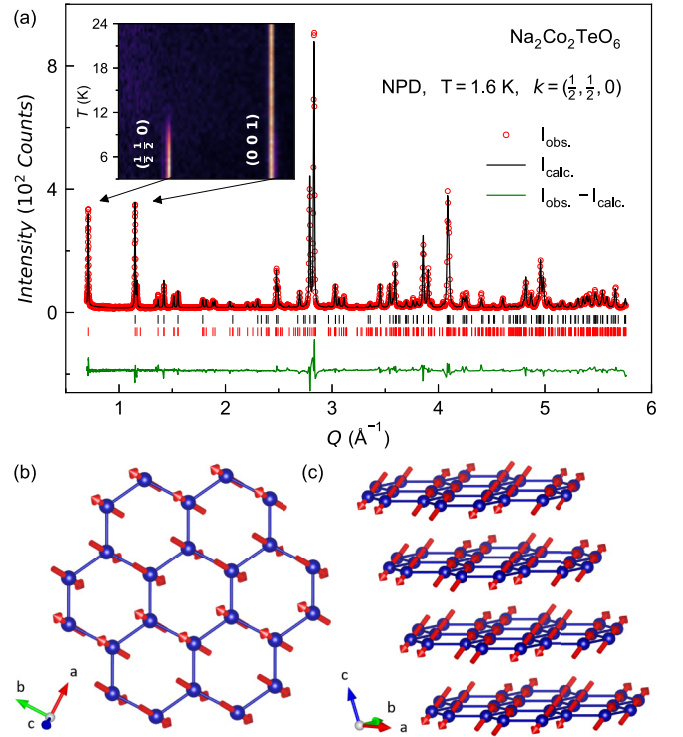
the pseudospin-1/2 degrees of freedom above T_N. Table I compares the magnetic entropy of monoclinic $Na_2Co_2TeO_6$ with its hexagonal polymorph and the isostructural system $Na_3Co_2SbO_6$.

Figure 4(c) shows that the AFM transition is suppressed gradually by applying a magnetic field. Using the peaks in both dC/dT and $d\chi/dT$, a temperature-field phase diagram is constructed in Fig. 4(d) that shows the suppression of the AFM order at 6 T. The measured C/T as a function of temperature shows similar behavior to the magnetic susceptibility and displays a suppression of the AFM peak with increasing field. However, in contrast to the complete change of behavior seen in χ at 6 T, the C/T data still shows a residual peak up to 9 T. Such a behavior is commonly observed in spin-glass and spin-liquid systems, for example in the hexagonal $Na_2Co_2TeO_6$ [38].

D. Neutron powder diffraction

To determine the nuclear and magnetic structures, NPD profiles were collected at 100 K [Fig. 2(b)] and 1.6 K [Fig. 5(a)]. The black and red ticks in Fig. 5(a) mark the positions of the nuclear and magnetic Bragg peaks, the latter of which appears at $T < T_N$. The inset of Fig. 5(a) compares a temperature-independent nuclear Bragg peak at

FIG. 5. (a) Neutron powder diffraction (NPD) pattern of the monoclinic $Na_2Co_2TeO_6$ at $T < T_N$ modeled by a zigzag magnetic structure visualized in the bottom panels. The black and red vertical bars correspond to the nuclear and magnetic Bragg peaks, respectively. The inset compares temperature dependence of a magnetic Bragg peak ($\frac{1}{2}\frac{1}{2}0$) and a nuclear peak (001) both indexed in the nuclear unit cell. (b) The spins are predominantly in the bc plane with 37° canting out of the ab plane. (c) The interlayer coupling is FM.

$Q = 1.2$ Å^{-1} to a temperature-dependent magnetic Bragg peak at $Q = 0.7$ Å^{-1} that appears below T_N.

The magnetic peaks in Fig. 5(a) are indexed by the commensurate propagation vector $\boldsymbol{k} = (\frac{1}{2}, \frac{1}{2}, 0)$. A magnetic symmetry analysis based on the structural space group $C2/m$ gives two magnetic maximal subgroups corresponding to the zigzag and stripy AFM orders within the honeycomb layers with FM coupling between the layers. However, the magnetic refinement for the zigzag order produces a higher-quality fit than the stripy configuration (Appendix C). Thus, the magnetic subgroup that best represents the experimental data is $P_s\bar{1}$ (irrep: mV_{1-}), which describes a zigzag AFM order within the layers and FM coupling between them [Figs. 5(b), 5(c)]. The nonvanishing $\chi(T)$ as $T \to 0$ and positive Θ_{CW} in Fig. 3(a) are consistent with such a magnetic structure.

A refinement of the moment size in the zigzag structure gives $\mu = (0.48(15), 1.50(15), 1.18(16))\,\mu_B$ suggesting that the spins lie primarily in the bc plane with $37°$ canting out of the ab plane [Figs. 5(b), 5(c)]. The magnetic moment per Co^{2+} from this refinement is $1.83\,\mu_B$ which can be understood by considering the high-spin configuration (^4F) of the $3d^7$ orbitals which splits into two triplets and a singlet ($^4F \to 2\,^4T +\,^4A$) under the octahedral CEF [53]. The lowest-energy triplet ^4T has an orbital angular momentum $L = -\frac{3}{2}L_{\text{eff}} = -\frac{3}{2} \times 1$ and spin $\frac{3}{2}$ leading to a total moment $\langle m \rangle = 2S + L = 2(\frac{3}{2}) - \frac{3}{2} = \frac{3}{2}$. This is close to but slightly lower than the observed moment of $1.83\,\mu_B$. The small difference is likely due to the trigonal distortion which is ignored in the first-order analysis.

IV. CONCLUSION

The results presented here highlight the interplay between structural symmetries and magnetic properties in honeycomb magnetic materials. Although both polymorphs of Na$_2$Co$_2$TeO$_6$ have similar Co-Te honeycomb layers, their structural space groups and magnetic properties are different (Table I). We highlight three important differences that may suggest stronger Kitaev interactions in the monoclinic polymorph compared to the hexagonal one. (i) Despite a comparable $|\Theta_{CW}|$, T_N is three times smaller in the monoclinic Na$_2$Co$_2$TeO$_6$ than in hexagonal polymorph, suggesting more frustration. (ii) Although both systems exhibit AFM ordering, Θ_{CW} is negative in the hexagonal polymorph but positive in the monoclinic one, indicating more anisotropy in the latter compound. (iii) Both systems have a zigzag order but the moments are canted out of plane in the monoclinic polymorph unlike the in-plane moments of the hexagonal polymorph.

It is important to note that Kitaev interactions are not always dominant in any Co^{2+} system with a honeycomb layered structure. Since SOC is weak in $3d$ transition metals, distortions of the local octahedral environment could alter the exchange interactions considerably [41]. For example, intralayer O-As-O and O-P-O bridges in BaCo$_2$(AsO$_4$)$_2$ and BaCo$_2$(PO$_4$)$_2$, respectively, and covalent interlayer O-Ti-O bonds in CoTiO$_3$ [Figs. 6(a), 6(b)] distort the local crystal field environment in favor of third-neighbor interactions (J_3) [42]. Consequently, the magnetic properties of these materials are better described by an XXZ model instead of the Kitaev
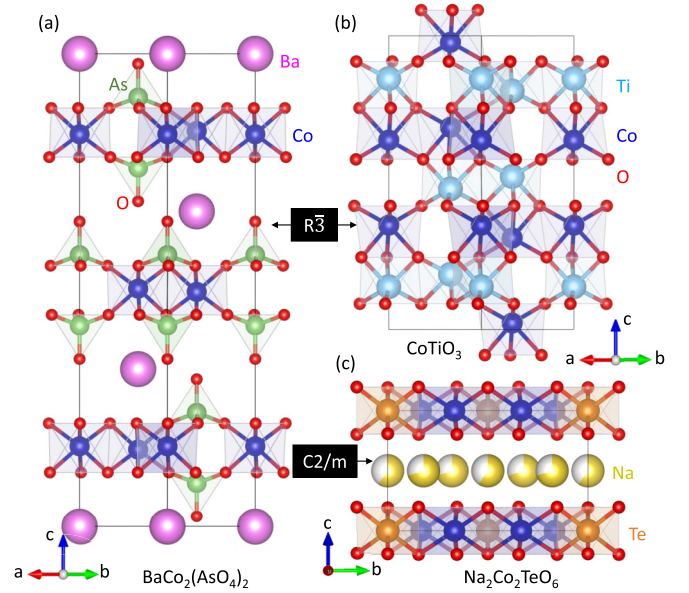

FIG. 6. (a) Crystal structure of BaCo$_2$(AsO$_4$)$_2$ in space group $R\bar{3}$ with intralayer O-As-O bridges. (b) Covalent interlayer O-Ti-O bonds in CoTiO$_3$ in space group $R\bar{3}$. (c) Monoclinic unit cell of Na$_2$Co$_2$TeO$_6$ in space group $C2/m$ without covalent intralayer bridges or covalent interlayer bonds [54].

model [42–46]. The title compound has ionic (instead of covalent) interlayer bonds and does not have intralayer bridges [Fig. 6(c)]; however, the Te atoms within the honeycomb layers could covalently bond to oxygens and modify the local crystal field environment. This will be the subject of future theoretical and experimental studies to determine which microscopic model, XXZ or Kitaev, best describes the ground state of the monoclinic Na$_2$Co$_2$TeO$_6$.

ACKNOWLEDGMENTS

TABLE II. Unit cell parameters of Na$_2$Co$_2$TeO$_6$ and quality factors of the PXRD Rietveld refinement at room temperature.

Unit cell parameters		Refinement parameters	
Space group	$C2/m$	Parameters	20
a (Å)	5.33225(6)	R_{Bragg} (%)	6.92
b (Å)	9.20808(8)	R_F (%)	5.57
c (Å)	5.80718(8)	R_{exp} (%)	5.38
β (deg)	108.90837(88)	R_p (%)	5.72
V (Å^3)	269.745	R_{wp} (%)	7.69
Z	2	χ^2	2.04
ρ (g cm^{-3})	4.770	T (K)	295

TABLE III. Atomic coordinates, site occupancies, and isotropic Debye-Waller factors from NPD Rietveld refinement of $Na_2Co_2TeO_6$ in space group $C2/m$ at 100 K.

Atom	Site	x	y	z	Occ.	B_{iso} (Å^2)
Na1	$4h$	1/2	0.32818	1/2	0.700	0.014
Na2	$2d$	0	1/2	1/2	0.600	0.014
Co1	$4g$	0	0.66923	0	1.000	0.007
Te1	$2a$	0	0	0	1.000	0.0002
O1	$8j$	0.28060	0.34569	0.80303	1.000	0.006
O2	$4i$	0.26474	1/2	0.19231	1.000	0.006

APPENDIX A: RIETVELD REFINEMENT

A co-refinement of PXRD and NPD patterns was used to accurately solve the crystal structure of monoclinic $Na_2Co_2TeO_6$. The unit cell parameters from the PXRD Rietveld refinement are summarized in Table II. Because neutron diffraction is more reliable in determining the oxygen positions, the atomic coordinates, Wyckoff-site occupancies, and Debye-Waller factors are reported from the NPD refinement in Table III. Since Na, Co, Te, and O have sufficiently different atomic form factors for neutron diffraction, the chemical composition of $Na_2Co_2TeO_6$ was reliably determined from the NPD refinement. Both the CIF and mCIF files for the monoclinic $Na_2Co_2TeO_6$ are included as Supplemental Material [54].

APPENDIX B: GOOD-QUALITY VS POOR-QUALITY SAMPLE

The quality of $Na_2Co_2TeO_6$ samples varies based on the amount of excess Na_2CO_3 and the temperature and duration of the synthesis. A common problem in poor-quality samples
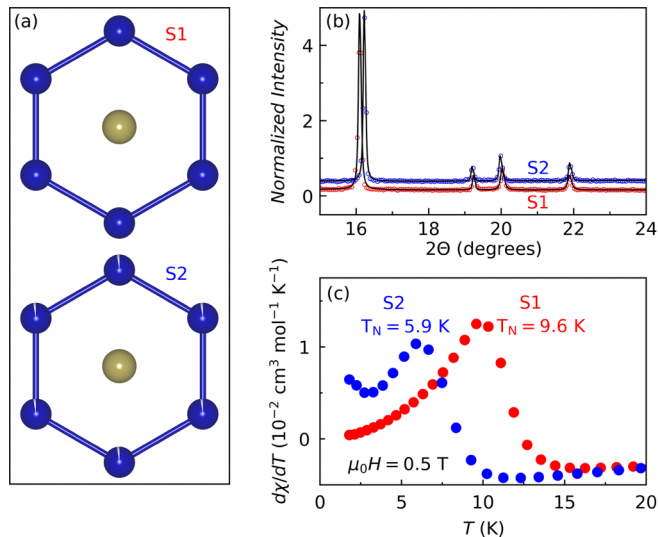

FIG. 7. (a) A good-quality sample (S1) does not have cobalt deficiency unlike poor-quality (S2) sample. (b) PXRD pattern of the poor-quality sample (S2) shows a shift of the first peak to the right indicating a larger c axis due to weaker interlayer bonding. (c) The magnetic transition is reduced from 9.6 to 5.9 K in the poor-quality sample.
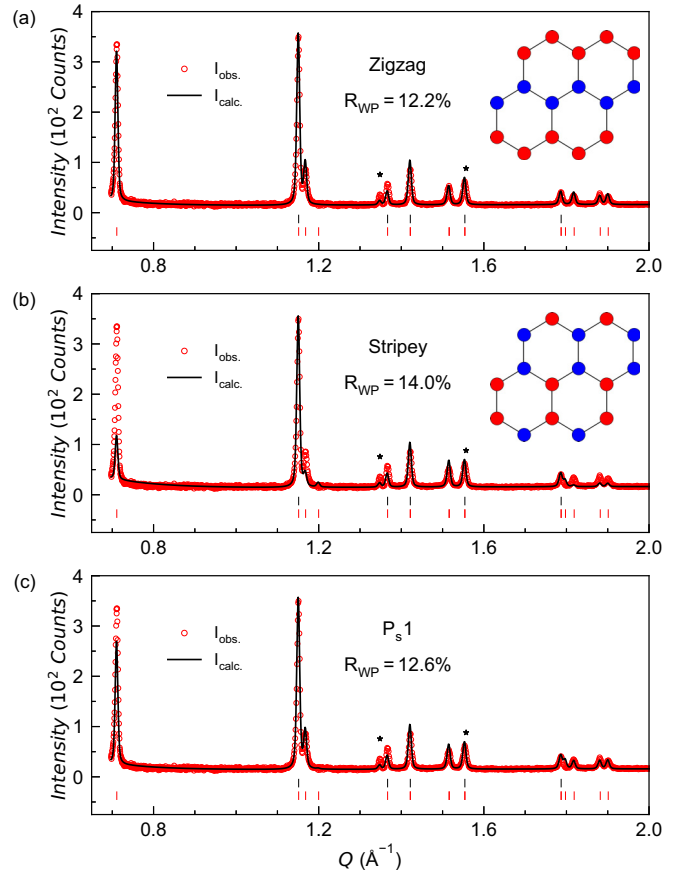

FIG. 8. Comparison between the magnetic Rietveld refinements of the NPD pattern using three different models. (a) Maximal magnetic space group $P_s\overline{1}$ with zigzag order, which gives the best fit and a moment of 1.83 μ_B per Co^{2+}. (b) Maximal magnetic space group $P_s\overline{1}$ with stripy order, which gives the worst fit. (c) Magnetic subgroup P_s1 with zigzag order but in a lower symmetry magnetic structure. The fit quality is worse than in panel (a). The red and blue circles in the insets represent antiparallel spins. The poor fit quality of the stripy model leads to a larger weighted profile factor R_{WP}. The asterisks mark the positions of Co_3O_4 impurity peaks.

is cobalt deficiency that is correlated with excess sodium between the layers (to maintain charge neutrality). Figures 7(a) and 7(b) show the results of the PXRD refinements in a good (S1) versus poor (S2) quality sample. The good quality sample (S1) has less sodium between the layers and no cobalt deficiency. The poor-quality sample (S2) has more sodium atoms between the layers which strengthen the interlayer bonds and shorten the c axis. Thus, the first Bragg peak in Fig. 7(b) is shifted to the right in S2 compared to S1.

Due to cobalt deficiency, T_N is shifted to a lower temperature in the poor-quality sample (S2) as seen in Fig. 7(c). Note that the T_N reduction in S2 is due to disorder; it is not an evidence of increasing proximity to the Kitaev spin-liquid phase. Also, there is an upturn in $\chi(T)$ of S2 at 3 K similar to the upturn observed in Fig. 3(b) in the hexagonal polymorph. It is likely that this upturn is due to disorder (Co deficiency) in the monoclinic phase and it shows up in hexagonal samples that are contaminated with a small amount of a parasitic monoclinic phase.

APPENDIX C: NEUTRON DIFFRACTION

A symmetry analysis of the $\boldsymbol{k} = (\frac{1}{2}, \frac{1}{2}, 0)$ wave vector in the structural space group $C2/m$ of $Na_2Co_2TeO_6$ gives two magnetic models belonging to the maximal magnetic space group $P_s\bar{1}$. The irreducible representations of these two magnetic models are mV_1^- and mV_1^+ corresponding to the zigzag and stripy orders, respectively. The Rietveld refinement for both magnetic structures is shown in Fig. 8. Whereas the zigzag model produces a good fit quality [Fig. 8(a)], the stripy model does not fit the data properly [Fig. 8(b)]. For example, the large Bragg peak at $Q = 0.7$ (Å^{-1}) and the small peaks near 1.8 and 1.9 (Å^{-1}) are fitted poorly in the stripy model. We found a small amount (2% volume fraction) of Co_3O_4 impurity in our samples. The peaks

corresponding to this impurity are marked by asterisks in Fig. 8.

It is also possible to refine the NPD pattern in a lower-symmetry space group P_s1 (irrep: mV_1^+) that allows four different Co moment sites, which we constrain to have the same size. The refinement in this model, which also gives a zigzag in-plane ordering but with $26°$ out-of-plane canting, is presented in Fig. 8(c). This model produces a lower-quality fit than the first zigzag model in Fig. 8(a). It also gives a total moment of 2.91 μ_B which is considerably higher than the expected moment from the doublet ground state (1.5 μ_B) and should produce twice the magnetic entropy shown in Fig. 4(b). Thus, the model that best describes the behavior of the title compound is the zigzag model presented in Fig. 5 and Fig. 8(a).

[1] C. Broholm, R. J. Cava, S. A. Kivelson, D. G. Nocera, M. R. Norman, and T. Senthil, Quantum spin liquids, Science **367**, eaay0668 (2020).

[2] Y. Motome and J. Nasu, Hunting Majorana fermions in Kitaev magnets, J. Phys. Soc. Jpn. **89**, 012002 (2020).

[3] J. Knolle and R. Moessner, A field guide to spin liquids, Annu. Rev. Condens. Matter Phys. **10**, 451 (2019).

[4] L. Savary and L. Balents, Quantum spin liquids: A review, Rep. Prog. Phys. **80**, 016502 (2017).

[5] A. Y. Kitaev, Fault-tolerant quantum computation by anyons, Ann. Phys. **303**, 2 (2003).

[6] C. Nayak, S. H. Simon, A. Stern, M. Freedman, and S. Das Sarma, Non-Abelian anyons and topological quantum computation, Rev. Mod. Phys. **80**, 1083 (2008).

[7] A. Kitaev, Anyons in an exactly solved model and beyond, Ann. Phys. **321**, 2 (2006).

[8] Y. Singh, S. Manni, J. Reuther, T. Berlijn, R. Thomale, W. Ku, S. Trebst, and P. Gegenwart, Relevance of the Heisenberg-Kitaev Model for the Honeycomb Lattice Iridates A_2IrO_3, Phys. Rev. Lett. **108**, 127203 (2012).

[9] K. W. Plumb, J. P. Clancy, L. J. Sandilands, V. V. Shankar, Y. F. Hu, K. S. Burch, H.-Y. Kee, and Y.-J. Kim, α-$RuCl_3$: A spin-orbit assisted Mott insulator on a honeycomb lattice, Phys. Rev. B **90**, 041112(R) (2014).

[10] K. Mehlawat, A. Thamizhavel, and Y. Singh, Heat capacity evidence for proximity to the Kitaev quantum spin liquid in A_2IrO_3 (A = Na, Li), Phys. Rev. B **95**, 144406 (2017).

[11] I. I. Mazin, S. Manni, K. Foyevtsova, H. O. Jeschke, P. Gegenwart, and R. Valentí, Origin of the insulating state in honeycomb iridates and rhodates, Phys. Rev. B **88**, 035115 (2013).

[12] V. Todorova and M. Jansen, Synthesis, structural characterization and physical properties of a new member of ternary lithium layered compounds—Li_2RhO_3, Z. Anorg. Allg. Chem. **637**, 37 (2011).

[13] M. Abramchuk, C. Ozsoy-Keskinbora, J. W. Krizan, K. R. Metz, D. C. Bell, and F. Tafti, Cu_2IrO_3: A new magnetically frustrated honeycomb iridate, J. Am. Chem. Soc. **139**, 15371 (2017).

[14] F. Bahrami, W. Lafargue-Dit-Hauret, O. I. Lebedev, R. Movshovich, H.-Y. Yang, D. Broido, X. Rocquefelte, and F. Tafti, Thermodynamic Evidence of Proximity to a Kitaev

Spin Liquid in $Ag_3LiIr_2O_6$, Phys. Rev. Lett. **123**, 237203 (2019).

[15] F. Bahrami, E. M. Kenney, C. Wang, A. Berlie, O. I. Lebedev, M. J. Graf, and F. Tafti, Effect of structural disorder on the Kitaev magnet $Ag_3LiIr_2O_6$, Phys. Rev. B **103**, 094427 (2021).

[16] F. Bahrami, X. Hu, Y. Du, O. I. Lebedev, C. Wang, H. Luetkens, G. Fabbris, M. J. Graf, D. Haskel, Y. Ran, and F. Tafti, First demonstration of tuning between the Kitaev and Ising limits in a honeycomb lattice, Sci. Adv. **8**, eabl5671 (2022).

[17] J. H. Roudebush, K. Ross, and R. Cava, Iridium containing honeycomb delafossites by topotactic cation exchange, Dalton Trans. **45**, 8783 (2016).

[18] K. Kitagawa, T. Takayama, Y. Matsumoto, A. Kato, R. Takano, Y. Kishimoto, S. Bette, R. Dinnebier, G. Jackeli, and H. Takagi, A spin-orbital-entangled quantum liquid on a honeycomb lattice, Nature (London) **554**, 341 (2018).

[19] E. M. Kenney, C. U. Segre, W. Lafargue-Dit-Hauret, O. I. Lebedev, M. Abramchuk, A. Berlie, S. P. Cottrell, G. Simutis, F. Bahrami, N. E. Mordvinova, G. Fabbris, J. L. McChesney, D. Haskel, X. Rocquefelte, M. J. Graf, and F. Tafti, Coexistence of static and dynamic magnetism in the Kitaev spin liquid material Cu_2IrO_3, Phys. Rev. B **100**, 094418 (2019).

[20] J. Wang, W. Yuan, T. Imai, P. M. Singer, F. Bahrami, and F. Tafti, NMR investigation on the honeycomb iridate $Ag_3LiIr_2O_6$, Phys. Rev. B **103**, 214405 (2021).

[21] A. de la Torre, B. Zager, F. Bahrami, M. DiScala, J. R. Chamorro, M. H. Upton, G. Fabbris, D. Haskel, D. Casa, T. M. McQueen, F. Tafti, and K. W. Plumb, Enhanced hybridization in the electronic ground state of the intercalated honeycomb iridate $Ag_3LiIr_2O_6$, Phys. Rev. B **104**, L100416 (2021).

[22] G. Fabbris, A. Thorn, W. Bi, M. Abramchuk, F. Bahrami, J. H. Kim, T. Shinmei, T. Irifune, F. Tafti, A. N. Kolmogorov, and D. Haskel, Complex pressure-temperature structural phase diagram of the honeycomb iridate Cu_2IrO_3, Phys. Rev. B **104**, 014102 (2021).

[23] F. Bahrami, M. Abramchuk, O. Lebedev, and F. Tafti, Metastable Kitaev magnets, Molecules **27**, 871 (2022).

[24] A. de la Torre, B. Zager, F. Bahrami, M. H. Upton, J. Kim, G. Fabbris, G.-H. Lee, W. Yang, D. Haskel, F. Tafti, and K. W. Plumb, Momentum-independent magnetic excitation continuum in the honeycomb iridate $H_3LiIr_2O_6$, arXiv:2302.07907.

[25] J. Chaloupka, G. Jackeli, and G. Khaliullin, Kitaev-Heisenberg Model on a Honeycomb Lattice: Possible Exotic Phases in Iridium Oxides A_2IrO_3, Phys. Rev. Lett. **105**, 027204 (2010).

[26] H. Takagi, T. Takayama, G. Jackeli, G. Khaliullin, and S. E. Nagler, Concept and realization of Kitaev quantum spin liquids, Nat. Rev. Phys. **1**, 264 (2019).

[27] W. Witczak-Krempa, G. Chen, Y. B. Kim, and L. Balents, Correlated quantum phenomena in the strong spin-orbit regime, Annu. Rev. Condens. Matter Phys. **5**, 57 (2014).

[28] J. G. Rau, E. K.-H. Lee, and H.-Y. Kee, Generic Spin Model for the Honeycomb Iridates beyond the Kitaev Limit, Phys. Rev. Lett. **112**, 077204 (2014).

[29] R. Sano, Y. Kato, and Y. Motome, Kitaev-Heisenberg Hamiltonian for high-spin d^7 Mott insulators, Phys. Rev. B **97**, 014408 (2018).

[30] H. Liu and G. Khaliullin, Pseudospin exchange interactions in d^7 cobalt compounds: Possible realization of the Kitaev model, Phys. Rev. B **97**, 014407 (2018).

[31] P. P. Stavropoulos, D. Pereira, and H.-Y. Kee, Microscopic Mechanism for a Higher-Spin Kitaev Model, Phys. Rev. Lett. **123**, 037203 (2019).

[32] H. Liu, J. Chaloupka, and G. Khaliullin, Kitaev Spin Liquid in $3d$ Transition Metal Compounds, Phys. Rev. Lett. **125**, 047201 (2020).

[33] C. Wong, M. Avdeev, and C. D. Ling, Zig-zag magnetic ordering in honeycomb-layered $Na_3Co_2SbO_6$, J. Solid State Chem. **243**, 18 (2016).

[34] L. Viciu, Q. Huang, E. Morosan, H. Zandbergen, N. Greenbaum, T. McQueen, and R. Cava, Structure and basic magnetic properties of the honeycomb lattice compounds $Na_2Co_2TeO_6$ and $Na_3Co_2SbO_6$, J. Solid State Chem. **180**, 1060 (2007).

[35] J.-Q. Yan, S. Okamoto, Y. Wu, Q. Zheng, H. D. Zhou, H. B. Cao, and M. A. McGuire, Magnetic order in single crystals of $Na_3Co_2SbO_6$ with a honeycomb arrangement of $3d^7$ Co^{2+} ions, Phys. Rev. Mater. **3**, 074405 (2019).

[36] A. K. Bera, S. M. Yusuf, A. Kumar, and C. Ritter, Zigzag antiferromagnetic ground state with anisotropic correlation lengths in the quasi-two-dimensional honeycomb lattice compound $Na_2Co_2TeO_6$, Phys. Rev. B **95**, 094424 (2017).

[37] G. Xiao, Z. Xia, W. Zhang, X. Yue, S. Huang, X. Zhang, F. Yang, Y. Song, M. Wei, H. Deng *et al.*, Crystal growth and the magnetic properties of $Na_2Co_2TeO_6$ with quasi-two-dimensional honeycomb lattice, Cryst. Growth Des. **19**, 2658 (2019).

[38] W. Yao and Y. Li, Ferrimagnetism and anisotropic phase tunability by magnetic fields in $Na_2Co_2TeO_6$, Phys. Rev. B **101**, 085120 (2020).

[39] G. Lin, J. Jeong, C. Kim, Y. Wang, Q. Huang, T. Masuda, S. Asai, S. Itoh, G. Günther, M. Russina *et al.*, Field-induced quantum spin disordered state in spin-1/2 honeycomb magnet $Na_2Co_2TeO_6$, Nat. Commun. **12**, 5559 (2021).

[40] S. Mukherjee, G. Manna, P. Saha, S. Majumdar, and S. Giri, Ferroelectric order with a linear high-field magnetoelectric coupling in $Na_2Co_2TeO_6$: A proposed Kitaev compound, Phys. Rev. Mater. **6**, 054407 (2022).

[41] H. Liu, Towards Kitaev spin liquid in $3d$ transition metal compounds, Int. J. Mod. Phys. B **35**, 2130006 (2021).

[42] S. Das, S. Voleti, T. Saha-Dasgupta, and A. Paramekanti, XY magnetism, Kitaev exchange, and long-range frustration in the $J_{eff} = 1/2$ honeycomb cobaltates, Phys. Rev. B **104**, 134425 (2021).

[43] B. Yuan, I. Khait, G.-J. Shu, F. C. Chou, M. B. Stone, J. P. Clancy, A. Paramekanti, and Y.-J. Kim, Dirac Magnons in a Honeycomb Lattice Quantum *XY* Magnet $CoTiO_3$, Phys. Rev. X **10**, 011062 (2020).

[44] M. Elliot, P. A. McClarty, D. Prabhakaran, R. D. Johnson, H. C. Walker, P. Manuel, and R. Coldea, Order-by-disorder from bond-dependent exchange and intensity signature of nodal quasiparticles in a honeycomb cobaltate, Nat. Commun. **12**, 3936 (2021).

[45] H. S. Nair, J. M. Brown, E. Coldren, G. Hester, M. P. Gelfand, A. Podlesnyak, Q. Huang, and K. A. Ross, Short-range order in the quantum XXZ honeycomb lattice material $BaCo_2(PO_4)_2$, Phys. Rev. B **97**, 134409 (2018).

[46] T. Halloran, F. Desrochers, E. Z. Zhang, T. Chen, L. E. Chern, Z. Xu, B. Winn, M. Graves-Brook, M. B. Stone, A. I. Kolesnikov, Y. Qiu, R. Zhong, R. Cava, Y. B. Kim, and C. Broholm, Geometrical frustration versus Kitaev interactions in $BaCo_2(AsO_4)_2$, Proc. Natl. Acad. Sci. USA **120**, e2215509119 (2023).

[47] J. Rodríguez-Carvajal, Recent advances in magnetic structure determination by neutron powder diffraction, Phys. B: Condens. Matter **192**, 55 (1993).

[48] K. Momma and F. Izumi, *VESTA*3 for three-dimensional visualization of crystal, volumetric and morphology data, J. Appl. Crystallogr. **44**, 1272 (2011).

[49] J. Perez-Mato, S. Gallego, E. Tasci, L. Elcoro, G. de la Flor, and M. Aroyo, Symmetry-Based Computational Tools for Magnetic Crystallography, Annu. Rev. Mater. Res. **45**, 217 (2015).

[50] B. H. Toby and R. B. Von Dreele, GSAS-II: The genesis of a modern open-source all purpose crystallography software package, J. Appl. Crystallogr. **46**, 544 (2013).

[51] A. Banerjee, P. Lampen-Kelley, J. Knolle, C. Balz, A. A. Aczel, B. Winn, Y. Liu, D. Pajerowski, J. Yan, C. A. Bridges, A. T. Savici, B. C. Chakoumakos, M. D. Lumsden, D. A. Tennant, R. Moessner, D. G. Mandrus, and S. E. Nagler, Excitations in the field-induced quantum spin liquid state of α-RuCl$_3$, npj Quantum Mater. **3**, 8 (2018).

[52] Y. Motome, R. Sano, S. Jang, Y. Sugita, and Y. Kato, Materials design of Kitaev spin liquids beyond the Jackeli-Khaliullin mechanism, J. Phys.: Condens. Matter **32**, 404001 (2020).

[53] M. E. Lines, Magnetic properties of $CoCl_2$ and $NiCl_2$, Phys. Rev. **131**, 546 (1963).

[54] See Supplemental Material at http://link.aps.org/supplemental/10.1103/PhysRevB.108.064405 for both structural and magnetic crystallographic information files (CIF and mCIF) of the title compound.